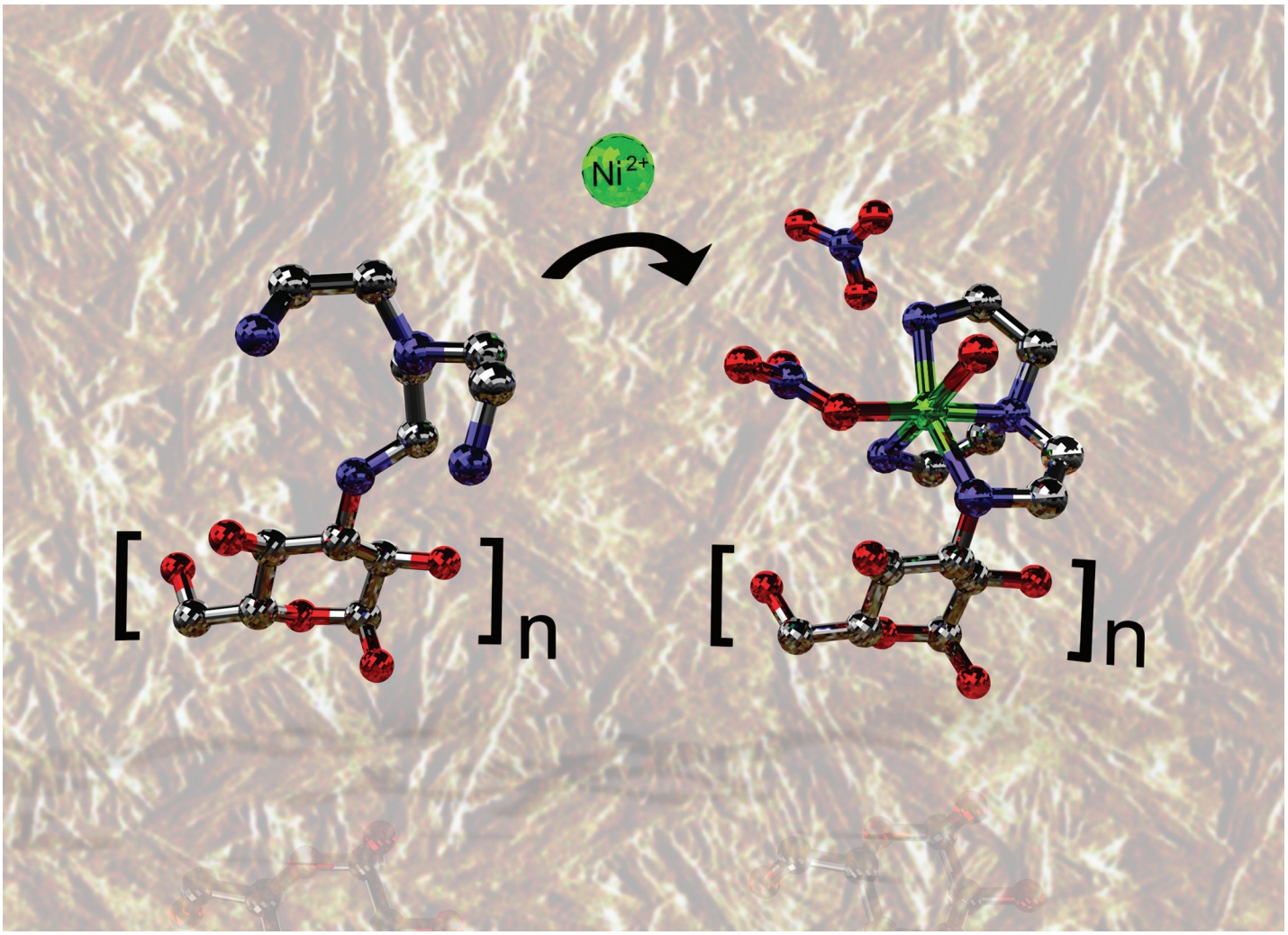

Showcasing research from Professor Gulaim A. Seisenbaeva's laboratory, Department of Molecular Sciences, Swedish University of Agricultural Sciences, Uppsala, Sweden.

Tailoring a bio-based adsorbent for sequestration of late transition and rare earth elements

Separation of Late Transition Metals (LTM) from Rare Earth Elements is principal challenge in recycling of magnetic materials from technical and electronic waste. Bio-based adsorbent material with enhanced selectivity towards LTM was produced by grafting a poly-amino ligand on a nano cellulose matrix. The material's mode of action was revealed *via* structural studies of relevant molecular model compounds.
Image reproduced by permission of Gulaim A. Seisenbaeva, Vadim K. Kessler and Adrian Dauphinee.

As featured in:

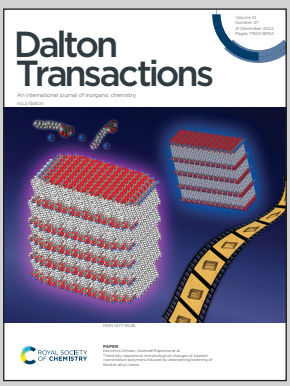

See Gulaim A. Seisenbaeva *et al.*, *Dalton Trans.*, 2022, **51**, 17978.

ROYAL SOCIETY OF CHEMISTRY

rsc.li/dalton

Registered charity number: 207890

Dalton Transactions

ROYAL SOCIETY OF CHEMISTRY

PAPER

View Article Online
View Journal | View Issue

Cite this: *Dalton Trans.*, 2022, **51**, 17978

Tailoring a bio-based adsorbent for sequestration of late transition and rare earth elements†

Troy C. Breijaert,[a] Tetyana M. Budnyak,[b] Vadim K. Kessler [a] and Gulaim A. Seisenbaeva *[a]

Received 28th September 2022,
Accepted 14th November 2022

DOI: 10.1039/d2dt03150g

rsc.li/dalton

The demand for new renewable energy sources, improved energy storage and exhaust-free transportation requires the use of large quantities of rare earth (REE) and late transition (LTM, group 8–12) elements. In order to achieve sustainability in their use, an efficient green recycling technology is required. Here, an approach, a synthetic route and an evaluation of the designed bio-based material are reported. Cotton-derived nano cellulose particles were functionalized with a polyamino ligand, tris(2-aminoethyl) amine (TAEA), achieving ligand content of up to *ca.* 0.8 mmol g^{-1}. The morphology and structure of the produced adsorbent were revealed by PXRD, SEM-EDS, AFM and FTIR techniques. The adsorption capacity and kinetics of REE and LTM were investigated by conductometric photometric titrations, revealing quick uptake, high adsorption capacity and pronounced selectivity for LTM compared to REE. Molecular insights into the mode of action of the adsorbent were obtained *via* the investigation of the molecular structure of the Ni(II)–TAEA complex by an X-ray single crystal study. The bio-based adsorbent nanomaterial demonstrated in this work opens up a perspective for tailoring specific adsorbents in the sequestration of REE and LTM for their sustainable recycling.

Introduction

Rare earth elements (REE) are critical elements for the development of modern technology and industries.[1,2] Their application in energy production and storage[3] in the form of magnetic materials, permanent magnets[4,5] and as components in NiMH batteries[6,7] has resulted in an increased demand for these materials.[2] This has resulted in an increase in an acquisition by mining, which is inherently unsustainable. In that regard, recycling the existing REE-containing materials such as common REE-based magnets needs to be promoted.[8–10] However, both mining and recycling require the use of extraction and separation techniques involving large amounts of hazardous reagents and solvents.[5,7,11] The most common technology for REE separation is acidic leaching with various acidic leaching agents, using several precipitation steps to remove unwanted components, after which the product can be calcined and re-dissolved.[5,12–14] However, most established methods require repeated steps to obtain the desired metal purity as it is difficult to separate REE from late transition metals (LTM, groups 8–12), which are commonly found with REEs in REE-containing recyclable materials.[15–17]

An alternative to the use of liquid-phase extraction and separation of REEs from late transition metals is the use of solid adsorbent materials for the extraction of metals from solution.[18] Today a wide range of adsorbent materials are available that can remove metals from solution, ranging from inorganic materials such as fly ash,[19] steel slag materials,[20] olivine and zeolites[21] to organic materials such as tree bark,[22] chitin/chitosan,[23–25] ion exchange resins, polymers,[26,27] protein-based adsorbents,[28,29] lignocellulosic sources[30] and peat.[31] With purely inorganic materials, it can be difficult to tune metal adsorption capacity and selectivity beyond what is inherent to the material but in some cases, at least with silicate materials[32–36] and metal oxides,[37,38] it is possible to graft the surface with organic ligands to improve metal uptake and selectivity. Organic adsorbents naturally contain reactive groups on the surface onto which ligands may be grafted. By choosing an appropriate type of coordinating ligand, it is possible to increase the adsorption capacity of the adsorbent materials and selectivity and therefore separate LTM from REE.[34,37] Creating a tailored ligand monolayer on the surface of the adsorbent opens up the possibility

[a]*Department of Molecular Sciences, Biocentrum, Swedish University of Agricultural Sciences, Almas Allé 5, Box 7015, SE-750 07 Uppsala, Sweden.*
E-mail: gulaim.seisenbaeva@slu.se
[b]*Division of Nanotechnology and Functional Materials, Department of Materials Science and Engineering, Uppsala University, Box 35, 751 03 Uppsala, Sweden*

†Electronic supplementary information (ESI) available. CCDC 2207506. For ESI and crystallographic data in CIF or other electronic format see DOI: https://doi.org/10.1039/d2dt03150g

to adjust it specifically for selective adsorption of target metal species, realizing the so-called molecular recognition approach.[39–41]

Natural bio-based polymer materials are especially suitable from an environmental point of view as they are considered renewable resources.[42–44] Cellulose, for example, is the most abundant, renewable polymer on the planet, accounting for several terra tons of annual biomass production.[45] It is found in plants as a major constituent, serving as a structural polymer, but it can also be produced by bacteria with the morphology depending on the source.[45,46] In addition, varying the original morphology depending on the source, cellulose can be processed in order to form more advanced structures such as networks, gels and fibres. In terms of the chemical structure, it consists of polymeric β-1,4-linked D-glucose which self-assembles into higher-order structures which can be chemically modified for specific applications.[47,48] The wide availability of cellulosic materials in nature combined with its renewable nature and low cost makes cellulose a very promising raw material for the preparation of advanced adsorbent materials.[49–51] By grafting the surface of cellulose with ligands that have high affinity to specific metals and preferentially binding them, the recycling and separation of magnetic and battery materials can be made more environmentally sustainable.[21,51] Amines, for example, are well known to strongly bind to late transition metals *via* the formation of coordinate covalent bonds while specific coordination geometries are known to stabilize certain metal cations. An example of such a ligand is tris(2-aminoethyl)amine, which contains four amino functions, three of which are located in freely rotating amine-containing arms and the ligand is known to form stable complexes with transition metals.[52–55]

In this study, we present the development and characterization of a cellulose-based nanoadsorbent material containing tris(2-aminoethyl)amine as a ligand that can rapidly form stable complexes with transition metals. Additionally, the mode of surface binding and possibility of ion exchange processes have been demonstrated by the single-crystal X-ray study of the model compound. The adsorption capacity, kinetics and metal uptake selectivity of REE and LTM and the pH-dependent desorption of metals from the produced cellulosic material have been studied.

Materials and methods

Synthetic procedures

Synthesis of cellulose nanocrystals. Cellulose nanocrystals (CNCs) were synthesized according to the literature procedure.[56] In short, 16 g of raw cotton was suspended in 140 mL of 64 wt% sulphuric acid at 45 °C for 45 minutes, after which it was poured into 10-fold excess water and allowed to settle. The supernatant was decanted and CNC suspension was poured into dialysis bags (MCWO = 12 kDa) and dialyzed against miliQ until the conductivity remained unchanged.

Synthesis of chlorinated nanocellulose. A CNC suspension corresponding to 3.0 g of CNCs (18.3 mmol AGU) was lyophilized and suspended in 60 mL of sieve-dried *N*,*N*′-dimethylformamide (DMF, 5 wt%) in a round-bottom flask and fitted with a reflux condenser and drierite-packed drying tube. The mixture was heated to 80 °C before adding 10.5 mL of thionyl chloride (145 mmol, 7–8 eq. based on AGU) dropwise over 15–20 minutes. The reaction was allowed to stir for 4 hours and the cellulose precipitated out in water, then it was neutralized with 3% ammonia solution until the pH became neutral. The resulting suspension was homogenized using a high-shear mixer (13 500 min^{-1}, 10 minutes). The particles were collected *via* centrifugation (10 min, 10k rpm) and washed several times with miliQ, re-suspending between each washing cycle. The sample was lyophilized for further analysis.

Synthesis of tris(2-aminoethyl)amine-cellulose. An aqueous, chlorinated cellulose suspension (1.5 g) was centrifuged, water was replaced with 1,4-dioxane, and washed 4 times. Particles were allowed to stand for some time before each washing cycle. Afterwards, the Cl-CNC suspension was transferred to a round-bottom flask, followed by the addition of 1.4 mL of tris (2-aminoethyl)amine (TAEA, 9.3 mmol, 2.2 eq. based on Cl content as determined by EDS), fitted with a reflux condenser and refluxed overnight. The product was collected *via* centrifugation, washed until the conductivity was similar to that of miliQ and lyophilized. The amine content was determined *via* conductometric titration. The approach is summarized in Scheme 1.

Synthesis of single crystals of model compounds

*[Ni(II)(TAEA)(H_2O)(NO_3)]NO_3 (**1**).* Ni(II)$(NO_3)_2 \cdot 6H_2O$ (279.8 mg, 1 mmol) was dissolved in 4 mL of miliQ, followed by the addition of 1 molar equivalent (143 μl) of the ligand and the

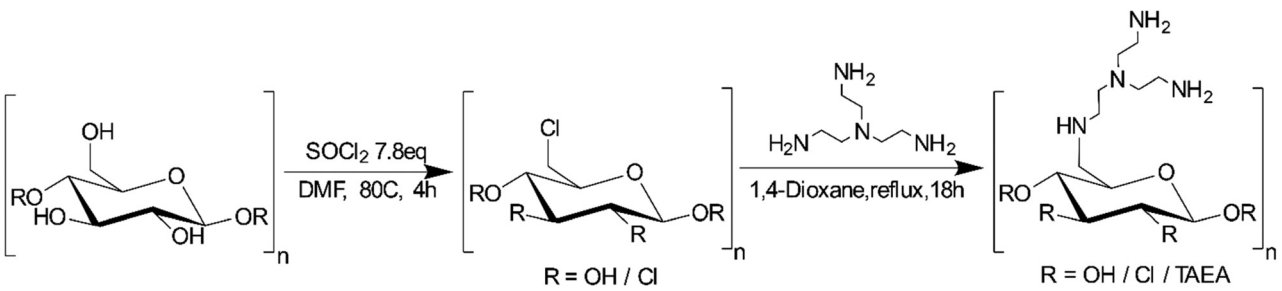

Scheme 1 Preparation route to the synthesis of tris(2-aminoethyl)amine modified cellulose.

solutions were allowed to slowly evaporate at room temperature, yielding violet block-shaped (prismatic) crystals.

*$[N(C_2H_4NH_3)_3](NO_3)_3$ (**2**).* 1 mmol of REE(III)$(NO_3)_2{\cdot}6H_2O$ (REE = Sm, Dy) was dissolved in 4 mL of miliQ, followed by the addition of 1 molar equivalent (143 μl) of the ligand, and the solutions were allowed to slowly evaporate at room temperature, yielding colorless plate-shaped crystals in a gel-like matrix.

Characterization

Scanning electron microscopy/energy dispersive X-ray scattering. Scanning electron microscopy (SEM) observations were conducted using a Hitachi FlexSEM 1000 at an acceleration voltage of 5 kV, a spot size of 20, and a working distance of 5 mm. For energy dispersive X-ray scattering (EDS), an acceleration voltage of 20 kV, a spot size of 50, and a working distance of 10 mm were used.

Atomic force microscopy. Samples were characterized using a Bruker Dimension FastScan Atomic Force Microscope (AFM) with a Nanoscope V controller in ScanAsyst mode using a Fastscan-B AFM probe (silicon tip, f_0: 400 kHz, k: 4 N m^{-1}, tip radius: 5 nm nominally) and a scan rate of 1–3 Hz. Data were processed using Gwyddion 2.56 with an aligned row median to remove skipping lines.

Fourier transform infrared spectroscopy. Fourier transform infrared (FTIR) analysis was performed with a Perkin-Elmer Spectrum 100 FT-IR spectrometer using KBr pellets.

Powder X-ray diffraction. Powder X-ray diffraction (PXRD) data were obtained on a Bruker D8 QUEST ECO diffractometer equipped with a proton area detector and graphite monochromated sealed-tube Mo-K_α (λ = 0.71073 Å) radiation source.

Single-crystal X-ray diffraction. Data collection was carried out with a Bruker SMART Apex-II diffractometer equipped with a graphite monochromated sealed-tube Mo-Kα (λ = 0.71073 Å) radiation source using omega-scans to obtain full hemisphere data down to 1.0 Å resolution (2theta − 50.05°). $C_6H_{20}N_6NiO_7$, mol. wt = 346.97 Da, monoclinic, space group $P2(1)/c$, a = 8.3129(6), b = 8.3129(6), c = 8.3129(6) Å, β = 91.8660(10)°, V = 1400.15(18) $Å^3$, and Z = 4. The structure was solved by direct methods. The coordinates of the majority of the non-hydrogen atoms were found from the initial solution and those for the residual non-hydrogen atoms and the hydrogen atoms of the water molecule attached to the nickel atom were determined in the subsequent difference Fourier syntheses. The coordinates of other hydrogen atoms were calculated using optimized geometric approximation. All non-hydrogen atoms were refined first in isotropic and then in anisotropic approximation. Hydrogen atoms attached to carbon atoms were refined isotropically, while for the H-atoms in the hydrating water molecules, only the coordinates were refined while the thermal deviation parameters were assumed to be equal to 1.500 times the atomic deviation parameters of the corresponding oxygen atom. The refinement converged at R_1 = 0.0836 and wR_2 = 0.1990 for 2049 observed reflections ($I > 2\sigma(I)$).

Nitrogen adsorption/desorption isotherms. The specific surface area and pore volume/area were determined from nitrogen adsorption/desorption isotherms on freeze-dried samples at −196 °C (Micromeritics ASAP 2020 Surface Area and Porosity Analyser, Norcross, GA, USA). The samples were degassed at 120 °C for 3 h before the measurements.

Conductometric titration. Titrations were performed using a Metrohm Titrando 888 (2.888.0310), fitted with an 856 conductivity module (2.856.0010), 800 Dosino (2.800.0010), 5-ring conductivity measuring cell (c = 0.7, 6.0915.100), using TIAMO Light 2.5 as automation software. Titers were determined using tris(hydroxymethyl)aminomethane (HCl) and potassium hydrogen phthalate (NaOH). Amine content was determined *via* conductometric titration by the back titration of protonated amine.

Photometric titrations. Metal sequestering titrations were performed by photometric titration using 5 mM ethylenediamine tetraacetic acid (EDTA). Prior to use, EDTA was standardized against calcium carbonate using eriochrome-T and ammonia buffer. Photometric titrations were performed in either acetate buffer with Xylenol Orange (Ln^{3+}) or ammonia buffer (pH 9) with murexide ($Ni^{2+}$and Co^{2+}).

Adsorption isotherms. For adsorption experiments, aminated samples were suspended in miliQ and the mass content was determined gravimetrically. 20 mg of cellulose was transferred to a 50 mL Falcon tube, followed by the addition of 20 mL of an appropriate metal stock (0.5, 1, 2, 3, 4, and 10 mM). Samples were left to equilibrate for 48 hours before collecting the particles *via* centrifugation and titrating the supernatant with 5 mM EDTA.

Adsorption kinetics. For adsorption kinetics experiments, 40 mg of an aminated cellulose sample was suspended in 40 mL of 10 mM of metal solution and samples were taken and titrated against 5 mM EDTA at predetermined intervals (15 min, 30 min, 1 h, 3 h, 6 h, 18 h, and 24 h).

pH-Dependent desorption. For pH-dependent desorption, 10 mg of the sample was suspended in 10 mL of 10 mM metal solution and allowed to equilibrate for 48 hours. The sample was centrifuged down and the metal solution was replaced with solutions of nitric acid with a predetermined pH and allowed to equilibrate for another 24 hours before centrifuging the particles and the supernatant was collected and titrated against 5 mM EDTA.5.

Results and discussion

Physical characterization of the adsorbent

Powder X-ray diffraction. The synthesis of tris-(2-aminoethyl) amine (TAEA) modified cellulose was performed by following a straightforward procedure. First, the substrate was made susceptible to nucleophilic substitution by chlorination with thionyl chloride in *N*,*N*-dimethylformamide. During the chlorination step, the accessible hydroxyl groups present on the AGU of cellulose were converted into chlorine ones, which then undergo nucleophilic substitution using one of

the amine groups present on TAEA to form the desired product.

One potential issue, depending on the application, with this approach, however, is that the chlorination of cellulose leads to a reduction of hydrogen-bonding along the solvent-accessible surface, which in turn allows the outer regions to dissolve in DMF. This will then precipitate out when exchanging solvent during washing or workup, leading to a change in morphology and crystallinity of the cellulose samples. The change in the cellulose structure as a result of reactive dissolution was clearly observed by pXRD (Fig. S1†). Here, we see a change in crystallinity and phase between pristine cellulose nanocrystals, composed of the Cellulose I phase, and the chlorinated product as a result of the reactive dissolution and subsequent regeneration of cellulose by precipitation in water. Further reaction of the chlorinated material with tris(2-aminoethyl)amine leads to a certain increase in crystallinity. X-ray patterns of modified products, as expected for a modified less crystalline polymer, showed essentially one broad peak with a slight shift to larger 2Theta due to the compression of hydrogen bonding as a result of the substitution of hydroxyl groups.

Textural characteristics of the cellulose–TAEA sample were investigated (Fig. S3†). Thus, the Brunauer–Emmett–Teller specific surface area (S_{BET}) was determined from the low-temperature nitrogen adsorption/desorption isotherms and found to be 11 $m^2\ g^{-1}$. The shape of the isotherm confirms the non-porous or macroporous surface of the material.[57] The pore-size distribution by volume and area was obtained using the Barret–Joyner–Halenda (BJH) method[58] by the desorption branch of the isotherms for the cellulose–TAEA sample. The BJH cumulative surface area and volume of pores between 1.7 nm and 300 nm were found to be 10.3 $m^2\ g^{-1}$ and 0.025 $cm^3\ g^{-1}$, whereas the BJH average pore width was 9.63 nm. Determination of the nano cellulose surface by nitrogen sorption is challenging because this material collapses, losing porosity even on freeze-drying that was applied. The data indicate that the surface of nano cellulose is not an active player in the adsorption process as the uptake seems to be related firsthand to the content of the functional ligand.

Fourier transform infrared spectroscopy (FTIR). In pristine cellulose nanocrystals derived from cotton by sulphuric acid hydrolysis, we can observe a strong broad peak at 3340 cm^{-1} (Fig. 1) which was attributed to OH stretch from hydroxyl present in cellulose and partly to moisture. Additionally, we observed several partly overlapping strong vibrations around 2910 cm^{-1} which were attributed to C–H stretching vibrations in the anhydroglucose backbone of the cellulose nanocrystals.

The relative position of most observed vibrations in the 3000–2800 cm^{-1} window remains essentially unchanged except for their transmission intensity, which may be attributed to the regeneration of the cellulose matrix observed *via* PXRD (Fig. S1†). After chlorination, a distinctly new peak appeared around 1725 cm^{-1}, which disappeared after amination. In addition, a small shift from 1650 to 1665 cm^{-1} was observed which may be attributed to N–H bend vibrations,

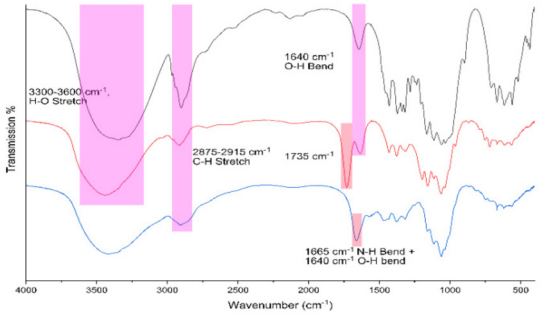

Fig. 1 FTIR spectrum of pristine cellulose nanocrystals derived from cotton by sulfuric acid hydrolysis (black), chlorinated CNCs from $SOCl_2$ in DMF (red) and TAEA-modified cellulose (blue).

indicating the successful grafting of tris(2-aminoethyl)amine onto the cellulose matrix.

Scanning electron microscopy (SEM)/energy dispersive X-ray scattering (EDS). This change in morphology observed by PXRD is further corroborated by AFM and SEM (Fig. 2A–F), in which we observed clear morphological changes between pristine CNCs derived from cotton and the final aminated product. In the original pristine CNCs, the rod-shaped CNCs (~40 × 150 nm, AFM, Fig. 2A and B) form ordered films with the cellulose self-assembling along the longitudinal direction of the crystal (Fig. 2A). Chlorination of the pristine CNCs by thionyl chloride in *N*,*N*′-dimethylformamide leads to a change in morphology where the product undergoes a transformation from rod-shaped CNCs into global cellulose nanoparticles as a result of reactive dissolution, followed by precipitation and

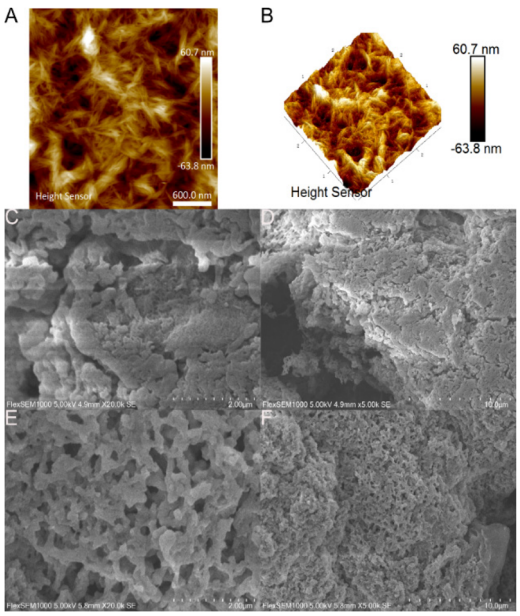

Fig. 2 AFM images of pristine CNCs derived from cotton by acid hydrolysis (A and B), and scanning electron microscopy images of chlorinated CNC derived from cotton CNCs in DMF (C and D) and TAEA-aminated cellulose (E and F).

high-shear mixing. Energy dispersive X-ray scattering (EDS) was used to analyse the surface composition of the materials. EDS analysis of the intermediate chlorinated product showed an appreciable chlorine content of approximately 2.81 ± 0.04 mmol g^{-1} for the chlorinated product. In an attempt to maintain the original CNC structure, we attempted to chlorinate lyophilized CNCs in dry toluene instead; however, this resulted in only very minor amounts of chlorine within the sample, in the range of 0.05 ± 0.02 mmol g^{-1}.

The resulting chlorinated product was aminated and after lyophilisation of the sample; the final product appeared to consist of globular nanoparticles in the 150–250 nm range. EDS analysis of the resulting aminated product showed an appreciable amine content of approximately 4.67 ± 1.55 mol g^{-1} nitrogen, corresponding to 1.17 ± 0.39 mmol g^{-1} amine. The resulting material still contains 1.76 ± 0.06 mmol g^{-1} chlorine and 0.12 ± 0.02 mmol g^{-1} sulphur in addition to the newly installed amine. The remaining chlorine in the sample may be attributed in part to the reaction being incomplete and in addition, partly attributed to the internalization of chlorine-containing cellulose chains, making it inaccessible for the subsequent amination step. For metal selectivity experiments, it is important to note the presence of elements not associated with the ligand as these may in turn interact with metal cations by coordinative covalent bonds or electrostatic interactions. Conductometric titration of the final aminated product leads to an amine content of 0.84 mmol g^{-1} (Fig. S2†). The discrepancy between EDS and conductometric titrations may be explained by the surface availability of the amine in aqueous media after lyophilisation, requiring a longer equilibration time.

Metal sequestration characterization

Adsorption characteristics. In order the evaluate the suitability of the material for metal sequestering in the recycling of REE-based materials, adsorption isotherms for the materials were measured using REE neodymium, samarium and the LTMs nickel and cobalt as these are commonly found in REE-based permanent magnets. The results showed that with the increasing initial metal concentration, the adsorption from solution increases until a maximum is reached due to the saturation of available surface binding sites (Fig. 3). The maximum adsorption capacities and the corresponding ligand stoichiometries can be found in Table 1.

Based on these results, the TAEA-modified cellulose material is promising for metal sequestering, obtaining near 1 : 1 ligand to metal stoichiometry, indicating that the adsorption capacity of the material is inherently tied to the ligand grafting, *i.e.* higher ligand grafting will increase the metal adsorption capacity.

To evaluate the rate at which metals are removed from solution, the adsorption kinetics were studied (see Fig. 4), which showed that for cobalt(II), the adsorption occurs rapidly, reaching 53% within an hour and 83% within 6 hours. The next metal with the highest rate of adsorption is neodymium, showing 40% adsorption in 6 hours, followed by nickel(II) at 34% in 6 hours. Samarium in comparison is rather slow to adsorb, reaching 61% adsorption in a 24-hour window. As cobalt(II) is rapidly adsorbed by TAEA-functionalized cellulose, it may provide some kinetic selectivity between the separation of cobalt from samarium in CoSm magnets and materials with similar compositions. The separation between nickel and neo-

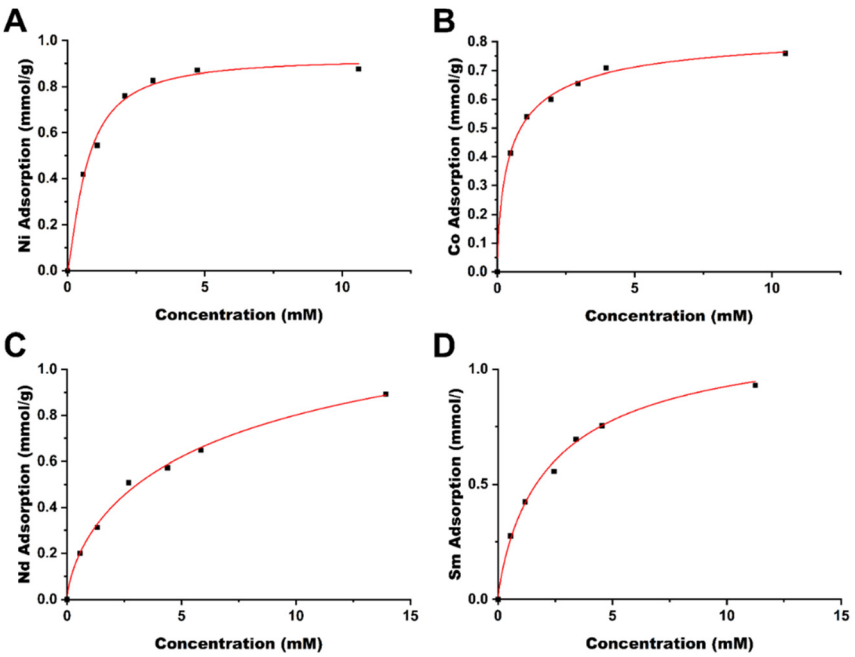

Fig. 3 Langmuir isotherms of late transition metals (A) Ni and (B) Co and rare earth elements (C) Nd and (D) Sm.

Table 1 Adsorption capacity and metal ligand stoichiometry of tris(2-aminoethyl)amine modified-cellulose

Metal	Adsorption capacity [mmol g^{-1}]	Metal/ligand stoichiometry
Co	0.76	0.90
Ni	0.88	1.04
Nd	0.79	0.94
Sm	0.82	0.97

Table 2 Metal selectivity by tris(2-aminoethyl)amine modified-cellulose as determined by EDS analysis of the adsorbent after equilibrating in equimolar aqueous metal mixtures

Metal mixture	Ratio
Ni : Co	1 : 1.1
Nd : Ni	1 : 5.1
Sm : Co	1 : 5.7
Sm : Nd	1 : 1.2

dymium in comparison, however, does not yield any significant kinetic selectivity.

As the intended purpose of the material is to selectively remove one class of metal (LTM/REE) from solution, the adsorption selectivity between equimolar mixtures of different metal ions by the material at a solution equilibrium was studied by EDS spectroscopy. By looking at the elemental ratios between metals on different spots we can estimate the average selectivity of the material. The result of EDS analysis can be viewed in Table 2. Briefly, when presented with an equimolar mixture between a lanthanide and a late transition metal, the TAEA functionalized material has a 5 : 1 preference towards the adsorption of late transition metals (Fig. S4 and S5†). When presented with an equimolar mixture of cobalt(II) and nickel(II), the product shows negligible selectivity towards cobalt (Fig. S6†). Similarly for a samarium(III)/neodymium(III) mixture, there is a negligible preference towards neodymium (Fig. S7†), indicating that the material is suitable for selectively adsorbing late transition metals over lanthanides from solution.

The difference between the adsorption kinetics of Sm(III) and Nd(III) is difficult to explain. It might originate from different features in the nucleation and growth of the corresponding hydroxides formed on the interaction of the ions with a local basic medium in the proximity of poly-amino ligands (please see below).

In addition, desorption tests were performed at pH values 0, 1, 2, 3, 4 and 5 using nitric acid in 50 mL Falcon tubes. After the samples were equilibrated for 48 hours, the samples were centrifuged and the pH was adjusted to predetermined values.

The samples were placed on an orbital shaker for 24 hours, after which the nanoparticles were separated by centrifugation

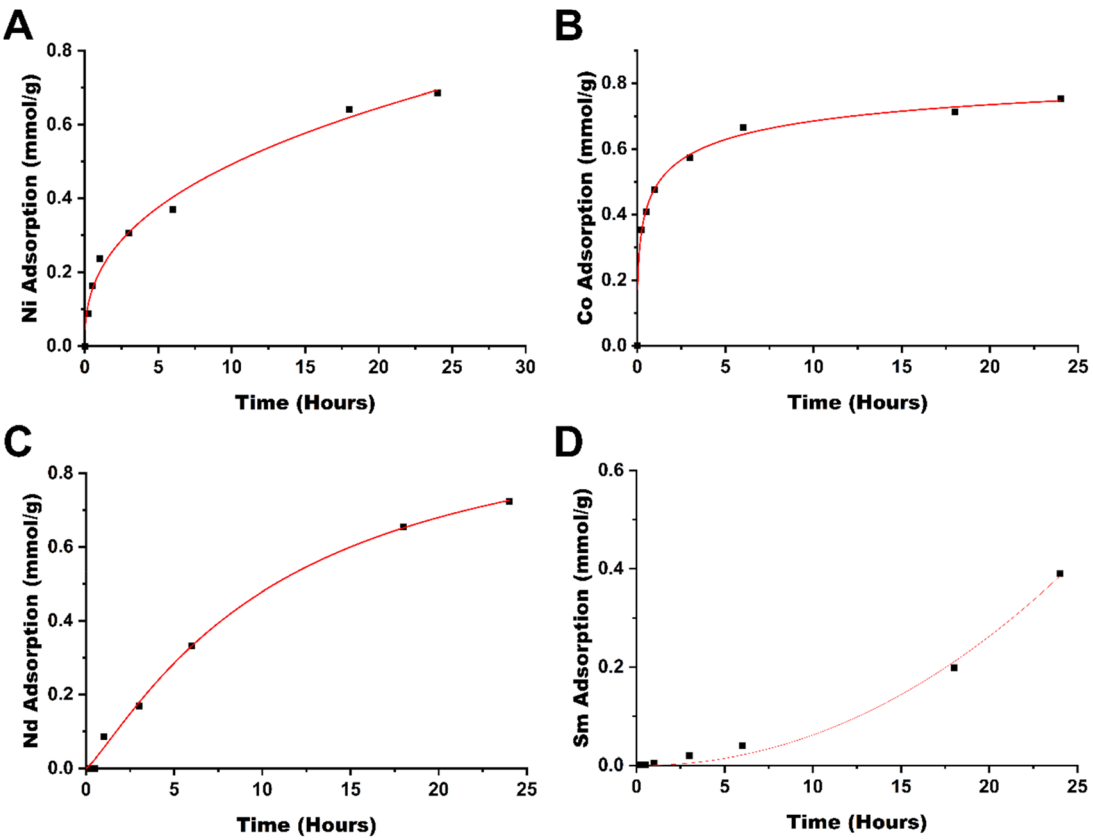

Fig. 4 Adsorption kinetics of (A) Ni, (B) Co, (C) Nd, and (D) Sm by cell-TAEA in a 24 h period.

(5500 rpm, 10 min), the supernatant was collected and the pH was adjusted with a base and titrated against EDTA to determine the desorbed metal amount. The results of the desorption experiments can be seen in Fig. 5 and are summarized in Table TS1.† For most metals at least 50% recovery is possible, expect for cobalt, which appears to be more resilient to acid treatment for recycling of the material.

Single-crystal X-ray diffraction. Aiming to get insights into possible metal complexes that may form on the surface of the modified cellulose in the presence of TAEA, attempts were made to grow X-ray-quality single crystals. In order to achieve this, solutions of the corresponding metals as nitrate salts were prepared in miliQ water, followed by the addition of 1 molar equivalent of the ligand and the solutions were allowed to slowly evaporate at room temperature in *ca.* 50% humidity, produced in the case of Ni(II) violet block-shaped crystals. The crystallization residue had a very uniform appearance, indicating complete conversion into a single complex form.

The single crystal X-ray study revealed a molecular structure (see Fig. 6), where the Ni(II) cation is octahedrally coordinated with the coordination sphere composed of the four nitrogen atoms of the TAEA ligand, one oxygen atom of the coordinated water molecule and one more oxygen atom from the inner-sphere coordinated nitrate ion. The bond lengths are essentially equivalent for all the Ni–N contacts (Ni(1)–N(2) 2.085(6), Ni(1)–N(3) 2.109(6), Ni(1)–N(4) 2.072(6), and Ni(1)–N(5) 2.095(6) Å) and the coordinated nitrate oxygen atom (Ni(1)–O(1) 2.101(5) Å). The bond to hydrating the water molecule is considerably longer, Ni(1)–O(1B) 2.201(5) Å, which is a commonly observed feature. Bonding within the Ni(TAEA) fragment is comparable with that observed earlier in the structures of Ni(II) with this ligand such as $Ni(TAEA)(NO_3)_2$ [54] and $[Ni_3(TAEA)_4(H_2O)_2(TMEDA)_2]Cl_6$.[59] In these latter structures, the nature of bonding was very analogous with essentially equal bonds to the five neighbours, four N-atoms of the TAEA ligands in both cases (Ni–N 2.055–2.095 and 2.080–2.117 Å respectively) and one more atom – either an O-atom in one of the nitrate ligands or a N-atom of the additional TMEDA ligand (2.075 Å in both cases). The sixth bond is much longer and stays for bonding either to an oxygen atom in an additional nitrate ion or to that in a water molecule. Observation of this manner of bonding actually is rather peculiar, indicating the most probable Jahn–Teller effect in the $3d^8$ configuration of the Ni(II) cation, resulting in the weakening of one bond in the octahedral coordination sphere permitting facile ligand exchange between the hydrating water and the nitrate ligand (Table 3).

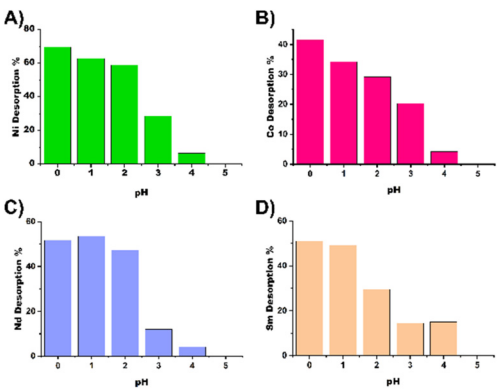

Fig. 5 pH-Dependent desorption of (A) Ni, (B) Co, (C) Nd and (D) Sm from cell TAEA.

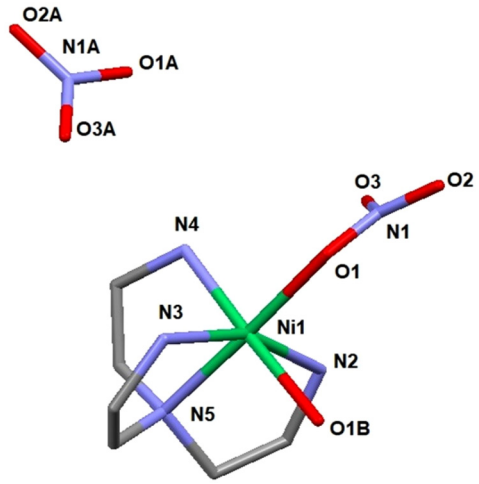

Fig. 6 Molecular structure of $[Ni(TAEA)(H_2O)(NO_3)](NO_3)$ (**1**).

Crystallization in a more humid environment in this case led to a structure with the water molecule included in the coordination sphere and "free" nitrate ion. The late transition metal cations (an analogous Co(II) structure has been reported with two nitrite ligands bound in the coordination sphere *via* N-atoms, $Co(TAEA)(NO_2)_2$ [55] – all bonds essentially equal in length) are apparently forming stable complexes with the chelating TAEA ligand, which explains the stronger selectivity of bonding towards Ni(II) and Co(II) compared to REE of the reported adsorbent.

In the case of REE, the product of mass crystallization from an equimolar mixture of metal nitrate and TAEA ligand

Table 3 Details of data collection and refinement for compound **1**

Compound	**1**
Chemical composition	$C_6H_{20}N_6NiO_7$
Formula weight	347.09
Crystal system	Monoclinic
Space group	$P2(1)/c$ (14)
R_1	0.0836
wR_2	0.1990
a [Å]	8.3129(6)
b [Å]	14.3595(11)
c [Å]	11.7358(9)
α [°]	90
β [°]	91.8660(10)
γ [°]	90
V [Å3]	1400.15(18)
T [K]	296(2)
Z	4
No. of obs. independent refl., $I \geq 2\sigma(I)$	2364
Residual electron density max	1.635

turned out to be solely $[N(C_2H_4NH_3)_3](NO_3)_3$ (**2**). The nature of the obtained product was the same for both Dy(III) and Sm(III) as indicated by unit cell parameter determination for multiple single crystals from the reaction mixture (see Table TS2 and Fig. S8†). The obtained structure is identical to that described by Bianchi *et al.*[60] This shows that the sorption mechanism of REE is supposedly principally different from that for LTM and is not involving inner sphere complexation with the grafted poly-amino ligand. The REE sorption may involve retention of either the hydrated cations or hydroxide forms. An additional argument for this option is provided by the work of Roesky *et al.*,[61] where the structures of several mixed-ligand complexes of Ni(II) and REE(III) with TAEA and Schiff base carboxylate were reported. In the competition between ligands, the Ni (II) cations were binding exclusively to nitrogen atoms in TAEA and REE – to the carboxylate oxygen atoms (see Fig. S9†). Such behavior is well in line with Pearson's hard and soft acid–base theory[62] as Ni(II) is a soft acid binding to a soft amino ligand, while REE cations are typically hard acids binding to hard oxygen donor bases.

Conclusions

The possibility of grafting a specific ligand permitting sequestration and separation of REE and LTM on a bio-based adsorbent matrix of nano cellulose has been demonstrated. Tris(2-aminoethyl)amine was attached to cellulose nanocrystals *via* a two-step route involving chlorination and amination steps. The morphology and crystallinity of the matrix were preserved, as demonstrated by PXRD and microscopy techniques. The produced adsorbent showed relatively quick adsorption kinetics at room temperature and pH = 6 for LTM, especially for Co(II), and considerably slower for REE. The adsorption capacity achieved values of *ca.* 0.8 mmol g^{-1}, corresponding to the functional ligand content and thus demonstrating the formation of surface complexes with 1 : 1 composition for all studied cations. The adsorbent revealed pronounced selectivity towards LTM compared to REE. The desorption of target cations was investigated as a function of pH, demonstrating comparably stronger retention of LTM compared to REE. The X-ray single crystal studies of molecular model compounds, $[Ni(TAEA)(H_2O)(NO_3)](NO_3)$ (**1**) and $[N(C_2H_4NH_3)_3](NO_3)_3$ (**2**), gave insights into the possible mode of action of the adsorbent and its cation and anion exchange processes.

Author contributions

Investigation, analysis, writing, and draft preparation – T. C. B.; Crystallography and writing – review and editing – V. G. K.; nitrogen adsorption/desorption and writing – T. M. B.; FTIR and AFM investigations, funding acquisition, and writing – review and editing – G. A. S.

Conflicts of interest

There are no conflicts to declare.

Acknowledgements

The authors would like to express their gratitude to Andreas Orthaber at Uppsala University for access to the single crystal X-ray diffractometer. In addition, the authors would like to express their gratitude to the Swedish Research Council STINT for the support of the grant Nanocellulose Based Materials for Environmental and Theranostic Applications and the Faculty of Natural Resources and Agricultural Sciences, SLU for the support of T. C. B.'s PhD position. The ÅForsk Research Foundation is gratefully acknowledged for the support of the grant Separation and Recycling of Rare Earth Elements and Nickel and Cobalt from magnets, ÅF 21-75.

References

1 J. B. H. Gordon, B. Haxel and G. J. Orris, Rare Earth Elements – Critical Resources for High Technology, **https://pubs.usgs.gov/fs/2002/fs087-02/**, (accessed 26/09/2022, 2022).
2 V. Balaram, *Geosci. Front.*, 2019, **10**, 1285–1303.
3 O. Serpell, W. Y. Chu and B. Paren, Rare Earth Elements: A Resource Constraint of the Energy Transition, **https://kleinmanenergy.upenn.edu/research/publications/rare-earth-elements-a-resource-constraint-of-the-energy-transition/**, (accessed 26/09/2022, 2022).
4 J. Cui, M. Kramer, L. Zhou, F. Liu, A. Gabay, G. Hadjipanayis, B. Balasubramanian and D. Sellmyer, *Acta Mater.*, 2018, **158**, 118–137.
5 Y. Yang, A. Walton, R. Sheridan, K. Güth, R. Gauß, O. Gutfleisch, M. Buchert, B.-M. Steenari, T. Van Gerven, P. T. Jones and K. Binnemans, *J. Sustainable Metall.*, 2016, **3**, 122–149.
6 A. Porvali, S. Ojanen, B. P. Wilson, R. Serna-Guerrero and M. Lundström, *J. Sustainable Metall.*, 2020, **6**, 78–90.
7 F. Holmberg, Licentiate, Chalmers University of Technology, 2017.
8 A. B. Patil, V. Paetzel, R. P. W. J. Struis and C. Ludwig, *Separations*, 2022, **9**, 56.
9 B. Deng, X. Wang, D. X. Luong, R. A. Carter, Z. Wang, M. B. Tomson and J. M. Tour, *Sci. Adv.*, 2022, **8**, eabm3132.
10 A. Porvali, V. Agarwal and M. Lundstrom, *Waste Manage.*, 2020, **107**, 66–73.
11 K. Korkmaz, M. Alemrajabi, Å. C. Rasmuson and K. M. Forsberg, *Sep. Purif. Technol.*, 2020, **234**, 115812.
12 S. Peelman, Z. H. I. Sun, J. Sietsma and Y. Yang, Presented in part at the 1st European Rare Earth Resources Conference, Milos, 07/09/2014, 2014.
13 R. Q. Honaker, W. Zhang and J. Werner, *Energy Fuels*, 2019, **33**, 5971–5980.

14 A. Yuksekdag, B. Kose-Mutlu, B. Zeytuncu-Gokoglu, M. Kumral, M. R. Wiesner and I. Koyuncu, *Environ. Sci. Pollut. Res. Int.*, 2022, **29**, 7772–7781.
15 M. Gergoric, C. Ekberg, M. R. S. J. Foreman, B.-M. Steenari and T. Retegan, *J. Sustainable Metall.*, 2017, **3**, 638–645.
16 N. Swain and S. Mishra, *J. Cleaner Prod.*, 2019, **220**, 884–898.
17 A. Rout and K. Binnemans, *Dalton Trans.*, 2014, **43**, 3186–3195.
18 Y. Hu, J. Florek, D. Lariviere, F. G. Fontaine and F. Kleitz, *Chem. Rec.*, 2018, DOI: 10.1002/tcr.201800012.
19 U. O. Aigbe, K. E. Ukhurebor, R. B. Onyancha, O. A. Osibote, H. Darmokoesoemo and H. S. Kusuma, *J. Mater. Res. Technol.*, 2021, **14**, 2751–2774.
20 H.-J. Kang, K.-G. An and D.-S. Kim, *J. Environ. Sci. Health, Part A: Toxic/Hazard. Subst. Environ. Eng.*, 2004, **39**, 3015–3028.
21 L. J. Westholm, E. Repo and M. Sillanpaa, *Environ. Sci. Pollut. Res. Int.*, 2014, **21**, 9109–9128.
22 S. Martini, S. Afroze and K. Ahmad Roni, *Alexandria Eng. J.*, 2020, **59**, 1637–1648.
23 S. Feng, X. Du, M. Bat-Amgalan, H. Zhang, N. Miyamoto and N. Kano, *Int. J. Mol. Sci.*, 2021, **22**, 3447.
24 D. L. Ramasamy, A. Wojtuś, E. Repo, S. Kalliola, V. Srivastava and M. Sillanpää, *Chem. Eng. J.*, 2017, **330**, 1370–1379.
25 D. C. da Silva Alves, B. Healy, L. A. A. Pinto, T. R. S. Cadaval Jr. and C. B. Breslin, *Molecules*, 2021, **26**, 594.
26 A. Chowdhury, S. K. Das, S. Mondal, S. Ruidas, D. Chakraborty, S. Chatterjee, M. K. Bhunia, D. Chandra, M. Hara and A. Bhaumik, *Environ. Sci.: Nano*, 2021, **8**, 2641–2649.
27 S. Mondal, S. Chatterjee, S. Mondal and A. Bhaumik, *ACS Sustainable Chem. Eng.*, 2019, **7**, 7353–7361.
28 Z. Dong, J. A. Mattocks, G. J. P. Deblonde, D. Hu, Y. Jiao, J. A. Cotruvo and D. M. Park, *ACS Cent. Sci.*, 2021, **7**, 1798–1808.
29 X. Xie, K. Yang, Y. Lu, Y. Li, J. Yan, J. Huang, L. Xu, M. Yang and Y. Yan, *J. Hazard. Mater.*, 2022, **438**, 129561.
30 M. L. Pitcher, B. Huntington, J. Dominick and A. Sheikhi, *Chem. Eng. J.*, 2022, **447**, 137418.
31 L. Ringqvist, A. Holmgren and I. Öborn, *Water Res.*, 2002, **36**, 2394–2404.
32 R. M. Ashour, M. Samouhos, E. Polido Legaria, M. Svärd, J. Högblom, K. Forsberg, M. Palmlöf, V. G. Kessler, G. A. Seisenbaeva and Å. C. Rasmuson, *ACS Sustainable Chem. Eng.*, 2018, **6**, 6889–6900.
33 E. Polido Legaria, I. Saldan, P. Svedlindh, E. Wetterskog, K. Gunnarsson, V. G. Kessler and G. A. Seisenbaeva, *Dalton Trans.*, 2018, **47**, 1312–1320.
34 A. Vardanyan, A. Guillon, T. Budnyak and G. A. Seisenbaeva, *Nanomaterials*, 2022, **12**, 974.
35 I. Anastopoulos, A. Bhatnagar and E. C. Lima, *J. Mol. Liq.*, 2016, **221**, 954–962.
36 D. Dupont, W. Brullot, M. Bloemen, T. Verbiest and K. Binnemans, *ACS Appl. Mater. Interfaces*, 2014, **6**, 4980–4988.
37 A. Mezy, A. Vardanyan, A. Garcia, C. Schmitt, M. Lakić, S. Krajnc, G. Daniel, A. Košak, A. Lobnik and G. A. Seisenbaeva, *Sep. Purif. Technol.*, 2021, **276**, 119340.
38 G. A. Seisenbaeva, I. V. Melnyk, N. Hedin, Y. Chen, P. Eriksson, E. Trzop, Y. L. Zub and V. G. Kessler, *RSC Adv.*, 2015, **5**, 24575–24585.
39 E. Polido Legaria, M. Samouhos, V. G. Kessler and G. A. Seisenbaeva, *Inorg. Chem.*, 2017, **56**, 13938–13948.
40 S. H. Gellman, *Chem. Rev.*, 1997, **97**, 1231–1232.
41 Y. M. Chen, C. Z. Wang, Q. Y. Wu, J. H. Lan, Z. F. Chai and W. Q. Shi, *Dalton Trans.*, 2021, **50**, 15576–15584.
42 N. Morin-Crini, S. Loiacono, V. Placet, G. Torri, C. Bradu, M. Kostić, C. Cosentino, G. Chanet, B. Martel, E. Lichtfouse and G. Crini, *Environ. Chem. Lett.*, 2018, **17**, 393–408.
43 D. Stewart, *Ind. Crops Prod.*, 2008, **27**, 202–207.
44 A. Boujemaoui, S. Mongkhontreerat, E. Malmstrom and A. Carlmark, *Carbohydr. Polym.*, 2015, **115**, 457–464.
45 D. Klemm, B. Heublein, H. P. Fink and A. Bohn, *Angew. Chem., Int. Ed.*, 2005, **44**, 3358–3393.
46 A. F. Jozala, L. C. de Lencastre-Novaes, A. M. Lopes, V. de Carvalho Santos-Ebinuma, P. G. Mazzola, A. Pessoa Jr., D. Grotto, M. Gerenutti and M. V. Chaud, *Appl. Microbiol. Biotechnol.*, 2016, **100**, 2063–2072.
47 A. C. O'Sullivan, *Cellulose*, 1997, **4**, 173–207.
48 K. H. Gardner and J. Blackwell, *Biopolymers*, 1974, **13**, 1975–2001.
49 R. D. S. Bezerra, R. C. Leal, M. S. da Silva, A. I. S. Morais, T. H. C. Marques, J. A. Osajima, A. B. Meneguin, H. da Silva Barud and E. C. da Silva Filho, *Molecules*, 2017, **22**, 2039.
50 O. Hamed, B. A. Lail, A. Deghles, B. Qasem, K. Azzaoui, A. A. Obied, M. Algarra and S. Jodeh, *Environ. Sci. Pollut. Res. Int.*, 2019, **26**, 28080–28091.
51 T. Oshima, K. Kondo, K. Ohto, K. Inoue and Y. Baba, *React. Funct. Polym.*, 2008, **68**, 376–383.
52 X. Huang, X. Chang, Q. He, Y. Cui, Y. Zhai and N. Jiang, *J. Hazard. Mater.*, 2008, **157**, 154–160.
53 A. Badiei, A. Mirahsani, A. Shahbazi, H. Younesi and M. Alizadeh, *Environ. Prog. Sustainable Energy*, 2014, **33**, 1242–1250.
54 D. Sivanesan, K. H. Song, S. K. Jeong and H. J. Kim, *Catal. Commun.*, 2019, **120**, 66–71.
55 M. K. Saha and I. Bernal, *C. R. Chim.*, 2007, **10**, 1170–1179.
56 M. S. Reid, M. Villalobos and E. D. Cranston, *Langmuir*, 2017, **33**, 1583–1598.
57 K. S. W. Sing, *Pure Appl. Chem.*, 1985, **57**, 603–619.
58 E. P. Barrett, L. G. Joyner and P. P. Halenda, *J. Am. Chem. Soc.*, 1951, **73**, 373–380.
59 K. Matelková, J. Moncol, R. Herchel, Ľ. Dlháň, R. Ivaniková, I. Svoboda, Z. Padělková and A. Mašlejová, *Polyhedron*, 2013, **56**, 1–8.
60 C. Bazzicalupi, A. Bencini, A. Bianchi, A. Danesi, C. Giorgi and B. Valtancoli, *Inorg. Chem.*, 2009, **48**, 2391–2398.
61 A. Bhunia, M. Yadav, Y. Lan, A. K. Powell, F. Menges, C. Riehn, G. Niedner-Schatteburg, P. P. Jana, R. Riedel, K. Harms, S. Dehnen and P. W. Roesky, *Dalton Trans.*, 2013, **42**, 2445–2450.
62 R. G. Pearson, *J. Am. Chem. Soc.*, 1963, **85**, 3533–3539.